CHEMISTRY OF MATERIALS

ARTICLE

pubs.acs.org/cm

Creation of Interior Space, Architecture of Shell Structure, and Encapsulation of Functional Materials for Mesoporous SiO_2 Spheres

Dan Ping Wang[†] and Hua Chun Zeng[*,†]

[†]Department of Chemical and Biomolecular Engineering, KAUST-NUS GCR Program, Faculty of Engineering, National University of Singapore, 10 Kent Ridge Crescent, Singapore 119260

Supporting Information

ABSTRACT: Over the past two decades, systematic development of preparative methodology for silica (SiO_2) based micro- and mesoporous materials has become a significant challenge for both fundamental science and advanced technology. In this work, we have developed a range of facile and versatile solvothermal methods for preparation of SiO_2 hollow spheres and their related nanocomposites at the submicrometer scale. First, we employ the concept of Ostwald ripening to generate interior space for porous SiO_2 spheres and prove this process is a simple, viable means to create large central cavities without using conventional hard or soft templates. Second, we devise a novel microemulsion system for synthesis of porous SiO_2 spheres using 1-dodecanethiol as a soft-template (i.e., micelles) to create interior spaces. Third, we architect complex double-shelled porous SiO_2 spheres by controlling the content of templating supramolecular assemblies. Along the synthesis of the phase-pure SiO_2 spheres, we have further developed two solution-based methods to introduce functional materials into the central spaces of the SiO_2 spheres; a total of 10 different core/shell nanocomposites have been made and investigated, which shows that these synthetic approaches indeed have a generality for design and architecture of the SiO_2-based porous materials. In addition to the materials synthesis carried out inside the central cavities, communicability of the cylindrical channels of the shells and enclosed inorganic and organic nanomaterials have also been tested with photocatalytic reactions and oxidative combustions. The spherical SiO_2 products can be broadly classified into five major architectural forms, and the mean diameter of the cylindrical channels in their shells are all uniformly in the range of 3.6−3.8 nm for the mesoporous products.

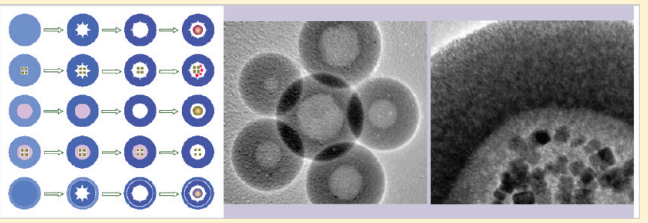

KEYWORDS: mesoporous silica, Ostwald ripening, hollow spheres, nanocomposites, nanocatalysts, core−shell reactors

1. INTRODUCTION

Encouraged by the discovery of MCM-41 in the early 1990s,[1] synthesis of porous silica (SiO_2) materials has since received tremendous research attention because of their many outstanding physicochemical properties such as large surface area, uniform pore size, low density, low dielectric constant, low refractive index, and good biocompatibility.[1−19] Over the past two decades, furthermore, the SiO_2-based micro- and mesoporous materials have been found to be very important in a vast field of technological applications, ranging from host materials for drug/gene delivery, heterogeneous catalysis, hard-templating for materials design and synthesis, novel adsorbents for heavy metal removal, to photonic devices and so on.[20−27]

In recent years, in particular, a massive work has been devoted to the synthesis of spherical SiO_2 with various pore structures.[28−39] Among them, SiO_2 spheres with one-dimensional (1D) cylindrical pores that are perpendicular to the spherical center are highly promising to work as "smart containers" for the above-mentioned applications, because these 1D-channels possess size-limiting "gates" and have the shortest traveling paths for any reactants and products or intercalates involved in a particular process. Despite the great success in recent research,[28−39] however, there are still many challenging issues to be further tackled. For example, uniform mesoporous SiO_2 spheres with hexagonally packed mesopores had been prepared at room temperature using conventional alkyl-trimethyl-ammonium-chlorides as templating molecules,[29] but their solid center may become a constraint to widen possible applications due to lacking a central working space. In order to generate an interior space, monodisperse SiO_2 spheres have been synthesized using a dual templating approach in which polystyrene (PS) beads were used as a hard template to create interior voids and cetyl-trimethyl-ammonium-bromide (CTAB) molecules were used as a soft template to form hexagonal pores for shells.[35] One technical drawback for this three-step approach is that the PS beads will have to be removed via calcination after synthesis. Apart from the inconvenience of post synthesis treatment, how to disperse the PS particles evenly in the reaction system is another crucial issue dictating the final morphology of SiO_2 hollow spheres. A simpler approach to synthesize SiO_2 hollow spheres with vertically perforated 1D-channels had been reported recently by using ethylene oxide (EO)−propylene oxide (PO) triblock copolymer [$(EO)_{20}(PO)_{70}(EO)_{20}$; P123] as a soft

Received: November 3, 2010
Revised: September 29, 2011
Published: October 18, 2011

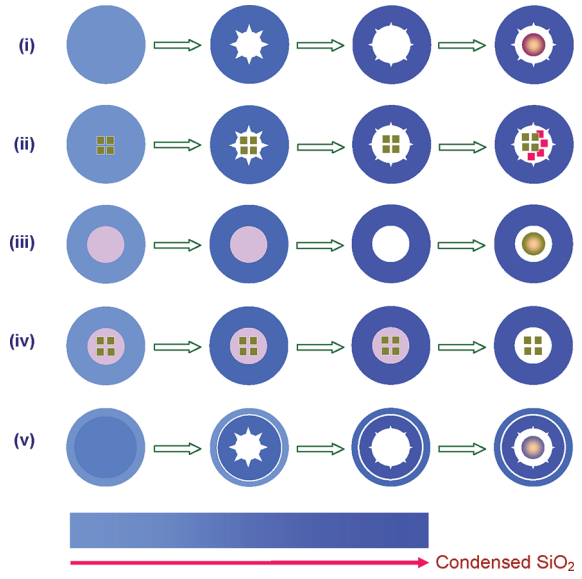

Figure 1. Schematic illustrations for some major synthetic routes developed to prepare mesoporous SiO_2 spheres and their derived products: (i) creation of interior space through Ostwald ripening, (ii) inclusion of nanoparticles into the central space while synthesizing SiO_2 hollow spheres with routes (i), (iii) generation of a smooth inner wall for the interior space through soft-templating (central micelles in light purple color), (iv) encapsulation of nanoparticles into the central space while preparing SiO_2 hollow spheres according to route (iii), and (v) architecture of double-shelled structures for SiO_2 hollow spheres. The SiO_2 phase is represented by a range of blue colors; a deeper color represents for a more condensed SiO_2 phase. Other processes extended from the above synthetic routes are described directly in the main text but not illustrated herein.

template and benzene as a swelling agent.[39] A much larger mesopore size around 7.7 nm could be obtained for SiO_2 shells with this approach after calcination, in comparison with those only using P123 but without benzene. However, an additional hydrothermal treatment was required in order to remove amorphous SiO_2 particles, which were formed during the sol−gel process involved, from the external surfaces of the spheres. Meanwhile, size and product morphology of SiO_2 spheres still need to be improved so as to be more suitable for further applications.[39]

In addition to preparing pure mesoporous silica solid or hollow spheres, synthesizing multifunctional core/shell nanocomposites represents another grand challenge in this research field.[40−52] In this type of multicomponent systems, for example, DNA biomolecules, proteins, enzymatic materials, transition-metal and noble-metal nanoparticles, metal-oxide nanoparticles, and so on have been encapsulated into the central spaces, while the mesoporous SiO_2 shells serve as controlled paths or gates to connect their enclosed interior materials to the outside space. With these functional materials, the mesoporous silica will become more robust and more versatile for applications. For instance, when magnetic nanoparticles of Fe_3O_4 are enclosed, the mesoporous SiO_2 spheres can respond rapidly to an external magnetic field, which provides an easy means for recovery of the spheres after use, in addition to the utilization of the intrinsic properties of enclosed matters.[49] Very recently, more complex shell structures have been engineered for this type of magnetic responsive silica spheres. For example, a sandwich structure of superparamagnetic spheres of Fe_3O_4@nSiO_2@mSiO_2 with perpendicularly aligned mesoporous 1D-channels has been prepared using CTAB as a soft-template to generate shell porosity and Fe_3O_4 as a core material for deposition of SiO_2 shells.[50] In spite of all the significant advancements, however, creation of an interior space, architecture of complex shell structure, and encapsulation of different functional materials still remain as three important research topics for general development of micro- and mesoporous materials,[8,9,12,40−53] including their derived nanocomposites.

Inspired by the previous works, in this article we report some of our recent research activities in synthesis of submicrometer SiO_2 spheres and related core/shell derivatives. Three different solvothermal approaches have been developed. First, we employ the concept of Ostwald ripening to generate interior space for porous SiO_2 spheres and prove this process is a simple, viable means to create large central cavities without using templates. Second, we devise a novel microemulsion system for synthesis of porous SiO_2 spheres using 1-dodecanethiol as a soft-template ("oil phase") to create interior space. Third, we architect complex double-shelled SiO_2 spheres by controlling the content of CTAB used in synthesis. Along the same line, we have further devised two solution-based methods to introduce functional materials into the central spaces of porous SiO_2 spheres, and a total of ten different kinds of core/shell composite structures have been prepared and investigated in this work, which shows that our synthetic methods are indeed facile and versatile and have generality for design and architecture of this class of materials. In addition to the materials synthesis carried out inside the central cavities, the communicable 1D-channels and enclosed functional materials have also been verified with photocatalytic reactions and oxidative combustions. Quite importantly, our hollow SiO_2 spheres and their derived nanocomposites can be broadly classified into five major architectural forms, as depicted in Figure 1, and the mean diameter of the 1D-channels on the SiO_2 shells are all controllable in a narrow range of 3.6−3.8 nm.

2. EXPERIMENTAL SECTION

2.1. Hollowing Mesoporous SiO_2 Spheres *via* Ostwald Ripening. In a typical synthesis, an amount of 0.2 g of cetyl-trimethyl-trimethyl-ammonium-bromide (CTAB, or named hexadecyl-trimethyl-ammonium-bromide, $C_{19}H_{42}BrN$, Fluka, ≥96.0%) was first dissolved in 25.0 mL of ethylene glycol (EG, C_2H_6O, Merck, ≥99.5%), followed by addition of 40−60 μL of tetraethyl orthosilicate (TEOS, $C_8H_{20}O_4Si$, Fluka, 99%) under vigorous magnetic stirring. After stirring for 5 min, 2.5 mL of diluted aqueous ammonia solution (6.4 wt %) was added into the above CTAB−EG−TEOS solution and kept stirring for another 5 min. The solution was then transferred to a Teflon-lined stainless steel autoclave. Solvothermal reactions were conducted at 100−180 °C for 1−6 h in an electric oven. The products of the reactions (i.e., mesoporous SiO_2 spheres; route (i), Figure 1) were later washed with ethanol twice and dried at 70 °C in an electric oven before materials characterization and other studies.

2.2. Hollowing Mesoporous SiO_2 Spheres *via* Soft Templating. In this type of synthesis, an amount of 0.2 g of CTAB was dissolved in 25.0 mL of EG solvent, followed by addition of 0.05−0.37 mL of 1-dodecanethiol (DDT, $C_{12}H_{25}SH$, Aldrich, 98%; which formed an "oil phase" for microemulsion). After an initial stirring (10 min), 60 μL of TEOS was added into the CTAB−EG−DDT solution under vigorous magnetic stirring. After stirring for another 5 min, 2.5 mL of diluted aqueous ammonia solution (6.4 wt %) was added into the above solution, and the stirring was continued for 5 more min. The solution was then transferred to a Teflon-lined stainless steel

dx.doi.org/10.1021/cm201631m |*Chem. Mater.* 2011, 23, 4886–4899

autoclave. Solvothermal reactions were carried out at 120 °C for 3−4 h inside an electric oven. In some experiments, furthermore, a small amount of sodium citrate dihydrate (0.10 g, $Na_3C_6H_8O_7 \cdot 2H_2O$, Aldrich, 99+%) was also added to the above reaction precursors in order to avoid intersphere aggregation. The products of the reactions (i.e., the SiO_2 spheres; route (iii), Figure 1) were then rinsed twice by ethanol and dried at 70 °C in an electric oven before further investigation.

2.3. Formation of Double-Shelled Mesoporous SiO_2 Spheres. In order to have some understanding of the role CTAB plays on the structure of mesoporous SiO_2 spheres, we also reduced the amount of CTAB used to 0.05 g in our synthesis, while keeping the remaining contents of reaction precursors identical to those used in Subsection 2.1. The mixture solution was later gone through the same solvothermal processes at 140−180 °C for 2−4 h. Double-shelled SiO_2 spheres were thus obtained with this reaction route (route (v), Figure 1).

2.4. Encapsulations of Functional Materials in Mesoporous SiO_2 Spheres. In this part of study, we had included several kinds of nanoparticles, ranging from organic to inorganic materials covering conducting polymers, semiconducting transition metal oxides and sulfides, transition metals, and noble metals, into the central spaces of mesoporous SiO_2 spheres. The following are 10 representative examples to illustrate two general methodologies developed.

Preinstallation Methods (TiO_2, Co_3O_4, ZnS, and Gold). A certain amount of TiO_2 (1.0 mg, P25, Degussa), Co_3O_4 (0.13−0.67 mg[54]), and ZnS (1.25 mg[55]) nanoparticles (which were synthesized according to previous literature reports[54,55]) was dispersed respectively into 2.0 mL of deionized water or 2.0 mL of aqueous solution of 0.10 g of sodium citrate dihydrate (to improve the dispersion of Co_3O_4 nanoparticles) followed by addition of 0.50 mL of concentrated aqueous ammonia solution (32 wt %). In the preparation of $Au@SiO_2$ core/shell material, 2.0 mL of red-wine color AuNPs suspension in deionized water (which was prepared according to a literature report[56]) was mixed with the same concentrated ammonia solution. Afterward, the synthesis of the SiO_2 spheres was carried out following the methods described in either Subsection 2.1 or 2.2. The products were later collected by centrifuging and washed twice with ethanol. Depending on the synthetic methods adopted, our samples are denoted with a reaction route (e.g., $TiO_2@SiO_2$ (route (ii); Figure 1) and $TiO_2@SiO_2$ (route (iv); Figure 1)).

On-Site Synthetic Methods (Polyaniline, Gold, and Silver). In order to add polyaniline (PAN) into a central space of mesoporous SiO_2 spheres, 20.0 mg of the as prepared mesoporous SiO_2 spheres (route (i) or (v); Figure 1) was dispersed in 30.0 mL of ethanol *via* sonication for 10 min. Later on, 50 μL of aniline (C_6H_7N, 99+%, Alfa Aesar) was added into ethanol and let it infiltrate into the mesopores with the assistance of 10 min of sonication. The polymerization process was initiated by addition of 1.0 mL of ammonium peroxydisulfate ($(NH_4)_2S_2O_8$, APS, 98%, Alfa Aesar) acidic solution (i.e., 0.156 g of APS was dissolved in 1.0 mL of 1.21 M hydrochloride acid). The reaction was carried out in a sonication bath for 4 h. The dark green product was washed 3 times by ethanol and dried in a vacuum electric oven at 40 °C overnight and the products are denoted as $PAN@SiO_2$ (route (i) or (v), Figure 1). In preparation of $Ag@SiO_2$ or $Au@SiO_2$ (route (i), Figure 1), furthermore, 5.0 mg of mesoporous SiO_2 spheres was soaked in 30.0 mL of 0.05 g of $AgNO_3$ or 0.03 g of $HAuCl_4$ ethanol solution under sonication for 10 min in order to let these noble metal salts infiltrate through their mesoporous channels; 0.2 g of PVP was also added into the $HAuCl_4$ ethanol solution to control the growth of Au nanoparticles. Each mixed solution was then transferred to a Teflon-lined stainless steel autoclave and reacted at 180 °C for a period of 2 to 3.3 h.

2.5. Calcination of Samples. The CTAB rod-like templates in the above three types of as-prepared SiO_2 spheres (routes (i), (iii) and (v), Figure 1) and in other nanocomposites such as $TiO_2@SiO_2$ (routes (i) and (iv), Figure 1) were removed *via* calcination in a programmed heating muffle oven before BET/BJH analyses, on-site synthesis of nanomaterials, and photocatalytic reactions of methyl orange degradation. Furthermore, the sample of $PAN@SiO_2$ nanocomposite was also calcined in order to prove the encapsulation of the polymer in the mesoporous SiO_2 (route (i) or (v), Figure 1) spheres. The general heating routine used to remove these organic phases (i.e., CTAB or PAN) is described as follows. The temperature was initially increased from room temperature to 150 °C at a rate of 5 °C/min. After 5 min at 150 °C, the temperature was further increased to 500 °C at a rate of 1 °C/min. The samples were kept at 500 °C for 60 min in order to remove the organic phases thoroughly.

2.6. Photocatalytic Reactions with Nanoreactors. In order to test the perforation of vertical pores of samples, we had carried out photoassisted deposition of gold nanoparticles and photocatalytic degradation of methyl orange ($C_{14}H_{14}N_3NaO_3S$) using calcined samples of $TiO_2@SiO_2$ (route (ii), Figure 1) and $TiO_2@SiO_2$ (route (iv), Figure 1), respectively. In photoassisted deposition of gold nanoparticles, 15 mg of $TiO_2@SiO_2$ powder sample (route (ii), Figure 1) was dispersed into 4.0 mL of ethanol in a glass sample vial, followed by the addition of 50 μL of 30 mM $HAuCl_4$ aqueous solution. Then the sample vial was sonicated for 5 min to have a good dispersion of mesoporous SiO_2 spheres. It was later placed into a dark chamber under UV irradiation (Hg lamp, 125 W, Philips; with a cutoff filter at λ = 360 nm) for 20 min. Product was collected by centrifugation for further study.

In the photocatalytic degradation of methyl orange, 10.0 mg of mesoporous $TiO_2@SiO_2$ spheres (route (iv), Figure 1; weight ratio TiO_2/SiO_2 = 1.3 mg/8.7 mg) synthesized *via* dual-templating method detailed in Subsection 2.4 were dispersed into 4.5 mL of 5 mg/L methyl orange solution. After magnetic stirring for 24 h, the solution was transferred into an UV−vis sample cell for photocatalytic reactivity test. The solid−solution mixture was illuminated by the Hg lamp (125 W, Philips; with a cutoff filter at λ = 360 nm) for 0.5 to 4 h. The concentration of the remaining reactant was then determined using UV−visible spectrophotometry (UV-2450, Shimadzu). In order to have a more accurate comparison, 1.3 mg of calcined P25 and 8.7 mg of mesoporous SiO_2 spheres (which were heat-treated under the same condition used for the $TiO_2@SiO_2$ sample) were physically mixed and tested for their photocatalytic reactivity so as to know the extent of hindrance of mesopores to the MO diffusion. Furthermore, 1.3 mg of pure free-standing P25 powder was also tested for its photocatalytic reactivity. Lastly, mesoporous SiO_2 spheres (heat-treated under the same condition used for the $TiO_2@SiO_2$ sample) without P25 was also examined so as to exclude the MO concentration drop caused by adsorption.

2.7. Materials Characterization. The ordered mesoporous structures of the as-prepared products were determined by X-ray diffraction and small-angle X-ray diffraction (XRD, XRD-6000, Cu K_α, Shimadzu) respectively. The structural and morphological information of all the nanoparticles and nanocomposites were obtained by transmission electron microscopy, high-resolution TEM (TEM, JEM-2010, and JEM-2100F, 200 kV, Joel) and field emission scanning electron microscopy (FESEM, JSM-6700F, Joel). Compositional investigation for some interested samples was carried out with Fourier transform infrared spectroscopy (FTIR, FTS-3500ARX, Bio-Rad) and X-ray photoelectron spectroscopy (XPS, AXIS-HSi, Kratos Analytical). The X-ray photoelectron spectra of the studied elements were referenced to the C 1s peak arising from adventitious carbon (its binding energy was set at 284.6 eV). The content of surfactant in silica was determined using thermogravimetric analysis (TGA, TGA-2050, TA Instruments). Specific surface area and porosity of the samples were determined with Brunauer−Emmett−Teller (BET) and Barrett−Joyner−Halenda (BJH) methods (NOVA-3000, Quantachrome Instruments) with adsorption and desorption of nitrogen gas.

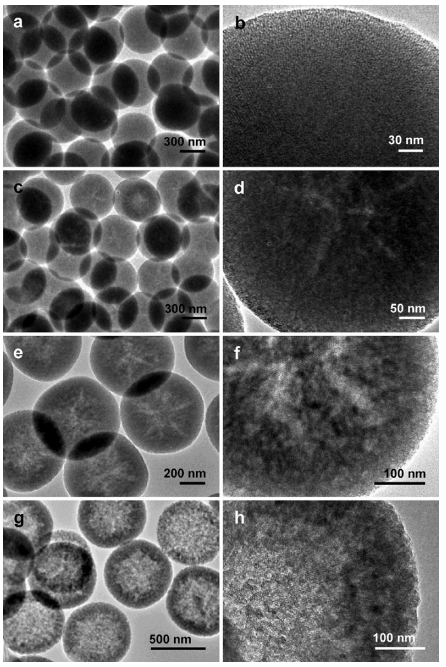

Figure 2. TEM/HRTEM images of mesoporous SiO_2 spheres prepared according to route (i) of Figure 1: (a-b) 100 °C for 3 h, (c-d) 120 °C for 2.3 h, (e-f) 120 °C for 4 h, and (g-h) 180 °C for 4 h.

3. RESULTS AND DISCUSSION

3.1. Creation of Interior Space *via* Ostwald Ripening. As described in Figure 1, under solvothermal conditions, five main types of mesoporous SiO_2 spheres with controllable interior spaces, nanomaterial inclusions, porosity, and shell architectures can be obtained from the developed processes. In particular, functional materials can be introduced into the central spaces of these mesoporous SiO_2 spheres through *preinstallation* or *on-site synthesis*. Such resultant systems, which should be viewed as complex multicomponent nanocomposites, may find new types of applications. For instance, they could be considered as catalyst-containing "membrane nanoreactors" for advanced heterogeneous catalysis, performing size selection for reactants and products. Further combinations and/or modifications of the above synthetic routes are still possible, which will also be addressed in later parts of this article.

TEM images of Figure 2 show a few evolutionary steps of creating interior spaces for the as-prepared SiO_2 spheres in accordance to route (i) of Figure 1. At 100 °C, solid SiO_2 spheres are readily formed with an average diameter of about 573 ± 14 nm (Figure 2a). A closer examination on the surface region reveals that there are straight mesopores formed perpendicularly to the center of the spheres (Figure 2b). At 120 °C, the star-shaped interior voids become observable while their overall spherical shape and the straight channel-like porosity remain largely unchanged (average sphere diameter 571 ± 18 nm, Figure 2c-d). After a longer ripening time (Figure 2e), the interior spaces can be observed more clearly in these SiO_2 spheres (average diameter 635 ± 38 nm, Figure 2e-f). At higher process temperatures, the evacuation of central solid can be accelerated. Large central spaces and large domains of highly ordered straight channels in hexagonal array are generated in the ripened spheres (average diameter 611 ± 13 nm, Figure 2g-h).

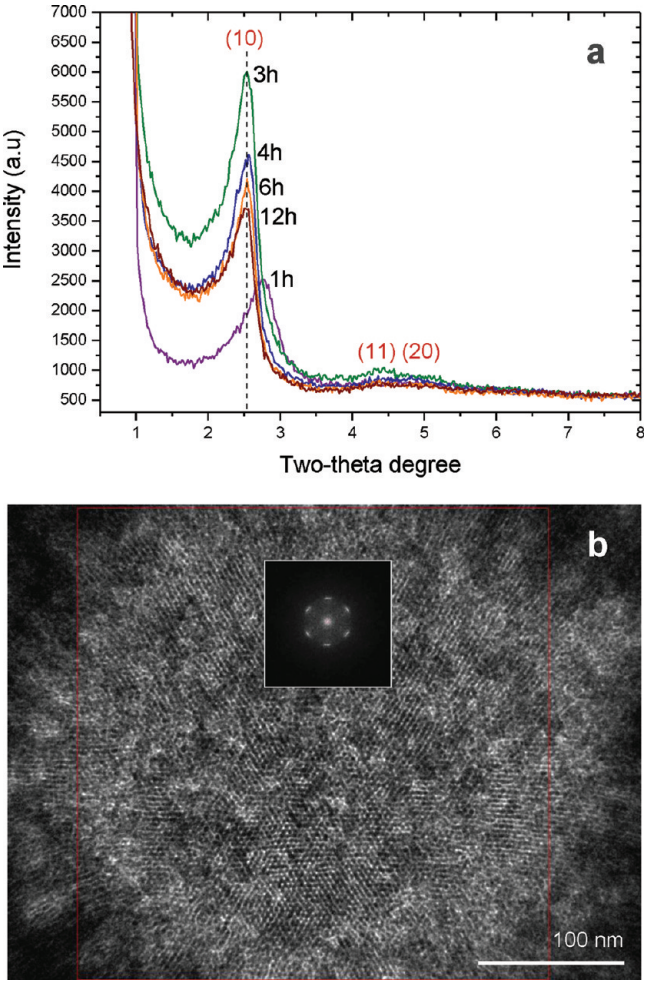

Figure 3. (a) XRD pattern evolution for the syntheses of mesoporous SiO_2 spheres at 120 °C over a time period of 1 to 12 h (route (i) of Figure 1) and (b) a HRTEM image and its related FFT pattern (inset) of SiO_2 sphere synthesized at 140 °C for 6 h (i.e., route (i) of Figure 1; also refer to SI-1 and SI-2).

Apart from varying the process temperature, we have also carried out two series of time-dependent experiments while keeping the process temperature constant. In Figure 3a (at 120 °C; the corresponding TEM images are given in Supporting Information SI-1a) and Table 1, one can find that the (10) interplane distance (d_{10}) of the 2D hexagonal symmetry (space group *p6m*) increases upon the ripening time from 1 h (d_{10} = 3.2 nm) to 3 h (d_{10} = 3.5 nm) and keeps essentially identical for longer process times (3 to 12 h). Moreover, there is an optimal ripening time of 3 h to attain the most highly ordered 1D-channel arrangement at this temperature, judging from the diffraction intensity of the (10) peak in the XRD patterns. By raising the temperature to 140 °C, the ripening process can be speeded up. However, it still took 6 h to obtain an equivalent product to that of Figure 2g-h (180 °C, 4 h). Figure 3b shows a HRTEM image at a high magnification for the above-mentioned sample (140 °C, 6 h); the average pore diameter is 3.6−3.8 nm (HRTEM image, SI-1b). The 1D-channels in hexagonal arrangement can be seen clearly, noting that these pores are parallel to the incident electron beam of TEM, and the FFT pattern produced from the central area of the image also confirms this structural feature. For those mesopores perpendicular to the electron beam of TEM, they

dx.doi.org/10.1021/cm201631m |*Chem. Mater.* 2011, 23, 4886–4899

Table 1. Properties of Some Representative Mesoporous SiO_2 Spheres in This Work

sample		d_{10} (nm)[a]	a_0[b]	surface area (m^2/g)[c]	pore radius (nm)[c]	pore diameter (nm)[c]
Figure 3	t = 1 h	3.2	3.7	-	-	-
	t = 3 −12 h	3.5	4.0	-	-	-
Figure 4	120 °C	3.5	4.0	951.1	1.9	3.8
	140 °C	3.5	4.0	603.9	1.9, 3.8	3.8, 7.6
	180 °C	3.5	4.0	125.0	1.9	3.8
Figure 7	DDT (50 μL)	4.5	5.2	760.0	1.8	3.6
	DDT (150 μL)	4.5	5.2	468.5	1.8	3.6
Figure 10	120 °C	3.6	4.2	924.9	1.9	3.8
	140 °C	3.6	4.2	421.1	1.9, 2.8	3.8, 5.6
	180 °C	3.6	4.2	137.5	1.9, 5.8	3.8, 11.6

[a] Interplanar spacing d_{10} of the as-prepared samples (with the presence of the organic phase CTAB). [b] Unit cell constant (a_0) of 2D hexagonal symmetry (in the space group *p6m*) calculated from d_{10}. [c] Specific surface areas, pore radius and diameter (determined by BET and BJH methods) for the calcined samples (i.e., after removal of the organic phase CTAB). See the Experimental Section.

are seen as "lines" projecting in all directions (around all 360° in the boundary areas of the image). The above observations on the formation of central interior space can also be explained by the Ostwald ripening mechanism.[57] Over the past seven years, this ripening process has been found operative in generating interior spaces for a great number of meso- and nanospheres of crystalline metal-oxides.[58−76] It should be mentioned that Ostwald ripening is not limited to only crystalline solids.[59] It is also operative in noncrystalline solids (such as sol−gels) and emulsion systems (e.g., milk, etc.) where molecules in small droplets tend to diffuse into large ones through the continuous phase of a suspension.[76] Consider the pristine silica particles that comprise a SiO_2 sphere in the present study. It is thought that the initial silica particles (or primary silica oligomers) formed from rapid hydrolysis and condensation reactions are small in size and there are plenty of interparticle spaces due to the stochastic aggregation and gelation. After the aggregation of these central silica particles, however, subsequently aggregated silica particles are relatively bigger because of continuous particle growth and fuller condensation (i.e., silicon species $Si(-O-Si\equiv)_n$ has a greater n value, where n = 0, 1, 2, 3, and 4) prior to their fractal aggregation. Therefore, there would be a particle size distribution along the radial direction of a SiO_2 sphere, that is, particles located in the inner parts of a SiO_2 sphere are generally smaller while those in the outer parts are larger in size. Because they are smaller and have higher surface energy, primary particles located in the central part are more reactive and will dissolve relatively easily. To achieve thermodynamic equilibrium, the inner silica particles will dissolve and regrow/deposit on outer silica particles which are normally with larger sizes, according to the Ostwald ripening mechanism (i.e., large particles were grown at the cost of smaller ones).[57] As evidenced in Figure 2 and Supporting Information (SI-1), higher reaction temperature and longer aging time apparently favor this matter relocation process from the inside out. Eventually, a hollow interior space can be created for the SiO_2 solid sphere. Note that the resulted silica phase in the outer region (shell) of a hollow sphere now becomes more continuous and thus more compact upon the ripening treatment, since the above-mentioned dissolution and recondensation of smaller primary particles also takes place preferentially in the junctures between silica particles or in the crevices of larger particle aggregates. Similarly, as evidenced in the XRD patterns of Figure 3a, the 1D-channels formed from supramolecular assemblies of CTAB molecules (the organic phase in the resultant SiO_2−CTAB hybrid) are also better aligned, that is they are better "crystallized" (i.e., better packed and aligned) after 3 h of reaction at 120 °C, accompanied with the observed condensation of the SiO_2 matrix phase. To the best of our knowledge, the findings presented in Figures 2 and 3 are the first example of hollowing amorphous solid spheres *via* the Ostwald ripening mechanism.[59,76]

To further address the factors dictating the above ripening process, Figure 4a compares the XRD patterns of three samples of mesoporous SiO_2 spheres synthesized at varying temperatures, while keeping the reaction time as a constant at 4 h. Judging by the diffraction intensities of (10) peaks, it is found that all samples possess similar interplane distance (d_{10} = 3.5 nm), but the regularity (the ordering) of mesopore is deteriorated with the increase of reaction time. In particular, the (10) peak of the 180 °C-synthesized sample becomes hardly recognizable. This result is also consistent with our TEM observation that a significant solid evacuation for the central hybrids takes place, and the profound structural reconstruction is associated with gel matrix condensation and relocation at this temperature (180 °C; Figure 2g-h; this observation will be further discussed in Figure 5 shortly). Specific surface area and porosity of the above samples were also measured with BET and BJH methods. The adsorption−desorption isotherms of liquid nitrogen for these samples are displayed in Figure 4b. These curves can be assigned to type IV isotherms with a typical H4 hysteresis loop according to IUPAC classification (which is associated with capillary condensation inside the pores).[53] Also listed in Table 1, the specific surface areas for the above mesoporous SiO_2 spheres are 951.1, 603.9, and 125.0 m^2/g, respectively. The substantial decrease in the specific surface area can be attributed to the condensation of SiO_2 gel structure which enlarges the central hollow space and shortens the 1D-channels within the SiO_2 spheres with a prolonged ripening time. Additionally, in Figure 4c, all three samples have a sharp pore radius of 1.9 nm (i.e., pore diameter 3.8 nm), indicating that the 1D supramolecular CTAB-assemblages serve as a template for the growth of perpendicular pores essentially does not change over the process temperature range from 120 to 180 °C.

In the above ripening process, we have observed it from TEM images that the initial void formation gives some polygonal shapes with their sharp corners projecting from the center of sphere (e.g., star-shaped voids with sharp corners, Figure 2). In association with the XRD patterns in Figure 4a, furthermore, the

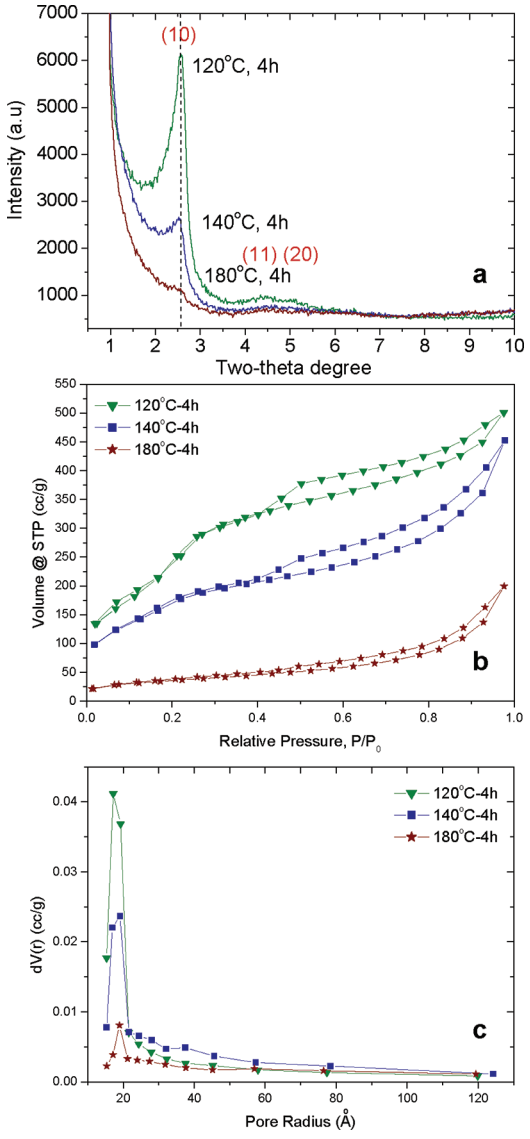

Figure 4. Characterization of mesoporous SiO_2 spheres synthesized at 120, 140, and 180 °C for 4 h according to route (i) of Figure 1: (a) XRD patterns (uncalcined samples), (b) nitrogen adsorption−desorption isotherms (calcined samples), and (c) pore radial distribution curves (BJH method).

evolution of the central space upon the solvothermal reaction temperature with the Ostwald ripening mechanism has also been investigated with the TEM technique, and the results have been given in SI-2 (4 h at 120, 140, and 180 °C, respectively). Interestingly, the number of polygonal edges in the central void space is gradually reduced with the ripening of the SiO_2−CTAB hybrid spheres. For example, both hexagonal and pentagonal central voids in the TEM images can be observed quite equally at 120 °C, but the pentagonal central voids become predominant at 140 and 180 °C. It should be recognized that the polygonal shapes observed in these TEM images indicate the formation of polyhedral central spaces in the SiO_2 spheres, and the reduction in the polygonal edges in (2D) TEM images would correspond to the reduction in the boundary planes of (3D) polyhedral central spaces, although the actual number of the boundary planes is difficult to be determined directly from the TEM images.

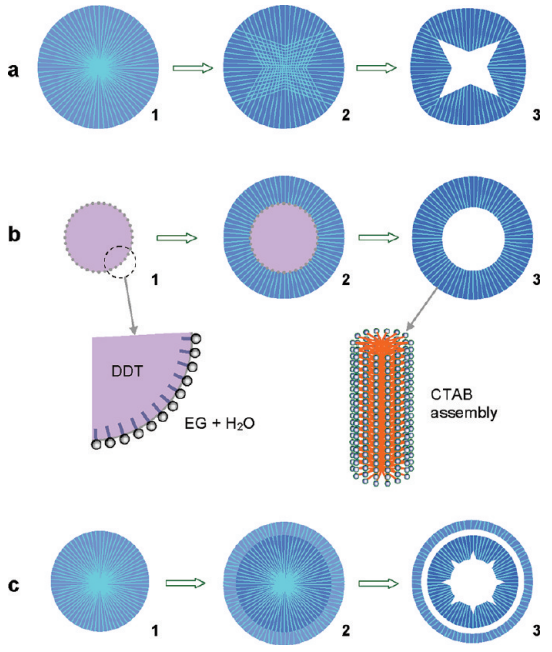

Figure 5. Schematic illustrations for formation processes of different interior spaces and shell structures of mesoporous SiO_2 spheres (refer to Figure 1): (**a**) route (i) − formation of solid SiO_2−CTAB hybrid (1), CTAB rod-like assemblies become more parallel upon aging (2), and evacuation of central SiO_2−CTAB due to stress (3); (**b**) route (iii) − formation of micelle (1), deposition of SiO_2−CTAB (2), and removal of soft templating micelle (3); and (**c**) route (v) − formation of SiO_2−CTAB core sphere (1), deposition of less ordered SiO_2−CTAB shell (2), and creation of spaces in the central core and interfacial region (3). Light green lines represent CTAB rod-shaped assemblies imbedded in the silica matrices.

In some cases at 180 °C, intriguingly, the original spherical SiO_2 turns into a "boxy sphere", giving rise to a cubelike central space (SI-2). The observed transformation of spherical SiO_2 to final cubical SiO_2 reveals a spontaneous tendency of surface flattening of mesoporous SiO_2 spheres. More specifically, there is clearly a strong driving force for 1D supramolecular assemblages of CTAB to achieve a more parallel alignment, as depicted in Figure 5a(1) to 5a(2), which would lead to interpenetration of the 1D-assemblies of CTAB form neighboring domains, noting that this interpenetration could cause severe stresses on the SiO_2 channels in the central region (Figure 5a(2)), and the SiO_2 gel phase in this overlapping region becomes more prone to ripening. Due to further gel condensation and thus shortening the SiO_2 mesopores, the observed pseudocubic space (and similarly other types of pseudo or irregular polyhedral space) results (Figure 5a(3)). Nonetheless, because of the significant reconstruction involved at a higher solvothermal temperature, the long-range order of the 1D-assemblies of CTAB could hardly be maintained, as had shown in the sample prepared at 180 °C of Figure 4. It should be pointed out that the amine-catalyzed dissolution of SiO_2 in ethylene glycol is unlikely associated with the observed hollowing process,[77] as this type of dissolution would have been started at the external surfaces where abundant ethylene glycol are in contact with the SiO_2 phase, noting that we did not use any organic amines or alkali hydroxides in the present study either.

3.2. Preparation of Smooth Inner Wall *via* Soft-Templating. It is noted that the surfaces of interior space in the above

dx.doi.org/10.1021/cm201631m |*Chem. Mater.* 2011, 23, 4886–4899

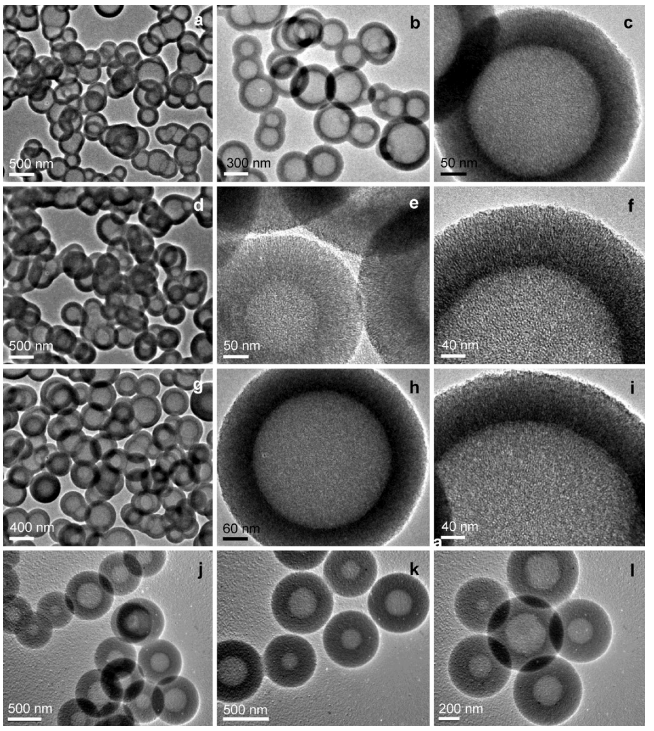

Figure 6. TEM images of mesoporous SiO_2 spheres prepared according to route (iii) of Figure 1: (a-c) with 0.2 g of CTAB + 0.37 mL of DDT at 120 °C for 4 h, (d-f) with 0.2 g of CTAB + 0.15 mL of DDT at 120 °C for 3 h, (g-i) with 0.05 g of CTAB + 0.37 mL of DDT at 120 °C for 3 h, and (j-l) with 0.1 g of sodium citrate + 0.2 g of CTAB + 0.05 mL of DDT at 120 °C for 3 h.

mesoporous SiO_2 spheres prepared through Ostwald ripening are generally not smooth owing to dynamical matter relocation involved in this nontemplating process. From a practical viewpoint, the uneven surfaces may provide a larger inner wall for distribution of desired functional materials, compared to a smoother inner surface. Moreover, uneven surfaces normally imply presence of more defect locations and thus more active sites. Geometrically, nevertheless, the shell thickness of these SiO_2 spheres is not constant, giving different traveling lengths for reactants and products inside and outside of this type of "nanoreactors" when chemical reactions are involved. From a fundamental viewpoint, therefore, it is also desirable to attain truly spherical mesoporous SiO_2 with constant shell thickness. To this end, we have found that if a small amount of alkanethiols (such as DDT; an oil phase) is introduced to the same EG−water system used in Subsection 3.1, hollow spheres of SiO_2 with a much smoother inner surface can be produced, as illustrated in Figure 1 (i.e., route (iii)). TEM images of some representative products with a perfect spherical central space according to this synthetic route are displayed in Figure 6. Because they do not mix well with the aqueous phase (EG−water), DDT molecules mainly serve as an oil phase in forming micelles in the resultant "oil-in-water" emulsion. Of course, since they also have a hydrophilic thiol headgroup, DDT molecules may also work as a surfactant, together with other organic molecules such as EG and/or CTAB in the interfacial regions between the oil and water phases, as described in Figure 5b, in which the thiol groups of DDT are expected to immerse into the EG−water phase. The resultant micelles then serve as a soft template for the deposition

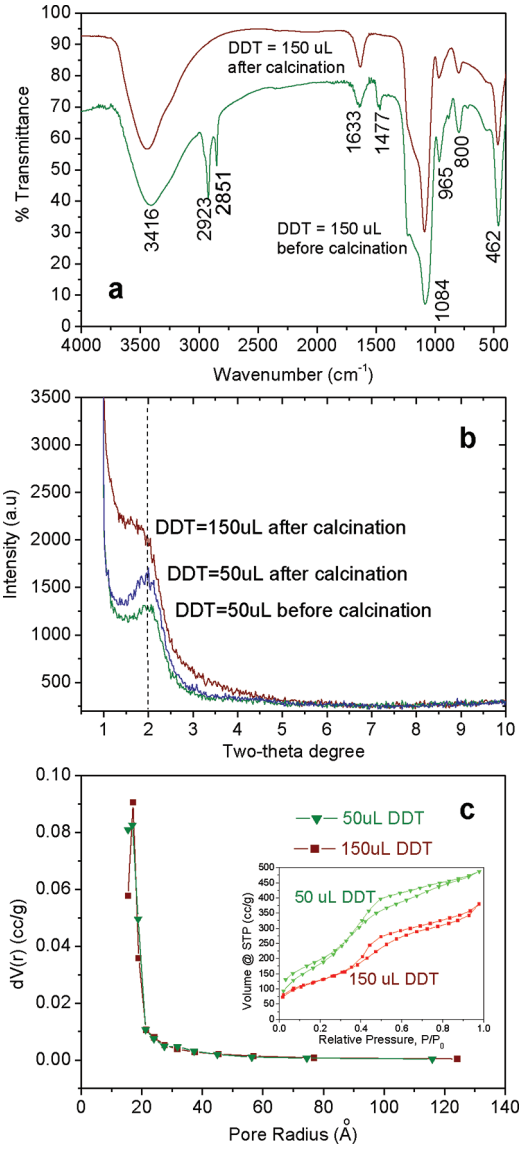

Figure 7. Characterization of mesoporous SiO_2 spheres prepared according to route (iii) of Figure 1: (a) Representative FTIR spectra of the as-prepared SiO_2 spheres before and after calcination, (b) XRD patterns (uncalcined samples), and (c) nitrogen adsorption−desorption isotherms (inset) and pore radial distribution curves (BJH method) of mesoporous SiO_2 spheres (calcined samples) synthesized with different amounts of DDT.

of SiO_2−CTAB hybrid shell (also refer to Figure 1(iii)). Illustrated in Figure 6j-l, when a small amount of sodium citrate is used in synthesis, interspherical aggregation can be eliminated entirely. In accordance to "oil/water" ratio in synthesis, furthermore, when less DDT is used, the central space of the SiO_2−CTAB spheres could also be reduced. This controllability has been elucidated in our products prepared using different starting precursors (e.g., Figure 6j-l, where the average sphere size is 663 ± 40 nm). Fourier-transform infrared (FTIR) spectra of Figure 7a show that in the as-prepared spheres (uncalcined sample), the asymmetric and symmetric vibrational modes of C−H are located at 2923 and 2851 cm^{-1} ($\nu_{as}(CH_2)$ and $\nu_s(CH_2)$).[78] The peak at 1477 cm^{-1} belongs to the scissoring mode (δ) of CH_2, indicating that the methylenes in the alkyl

dx.doi.org/10.1021/cm201631m |Chem. Mater. 2011, 23, 4886–4899

chains have an all-trans conformation,[78] which indeed confirms the inclusions of CTAB molecules in the SiO_2−CTAB hybrid spheres. On the other hand, the presence of the SiO_2 phase is evidenced in the asymmetric stretching, symmetric stretching, and bending vibrations of Si−O−Si are found at 1084, 800, and 462 cm^{-1} respectively. Furthermore, the IR absorption peak located at 965 cm^{-1} can be assigned to the stretching vibration of Si−O in the Si−OH bond, and the peaks at 1633 and 3416 cm^{-1} to the H_2O and −OH adsorbed on the surface of the SiO_2 phase.[79,80]

We have also investigated structural and surface properties of this set of hollow spheres. Shown in the XRD patterns of Figure 7b, in general, the hexagonal arrangement of 1D-assemblies of CTAB molecules in the shell structure is not as ordered as those reported in Figures 3a and 4a, and the hexagonal regularity observed in TEM images is less obvious when DDT is added (Figure 6), compared to those reported in Figures 2 and 3b. Nevertheless, pore structures of the silica phase are essentially identical before and after removal of the organic phase. In general, pore regularity is higher when a smaller amount of DDT molecules is included (50 μL), whereas that decreases when the amount of DDT used is greater ($\geq$150 μL). Both TEM (Figure 6) and XRD results (Figure 7b) indicate that there is an optimal amount of DDT for the controls of central space and pore structure. When it is overused, however, micelles formed by DDT molecules become more interconnected, as shown in Figure 6g-i. However, direct interruption to the hexagonal packing of the linear CTAB assemblages by entrapping DDT molecules can be ruled out on the basis of our XPS analysis (see SI-3 shortly). From Figure 7c, one could find that a larger surface area is obtained when the amount of DDT is reduced. This might be due to the smaller oil-droplets formed with less DDT in the emulsions. However, the DDT molecules will not alter the pore size of SiO_2 spheres which is shown by BJH pore radial distribution graphs in Figure 7c. The peaks of pore radial distribution are at the same position (1.8 nm, Table 1), suggesting that DDT molecules do not enter the 1D-assemblages of CTAB as a swelling agent to enlarge the cylindrical pores, but they are essential for the formation of central void spaces. In Figure 7c (inset), the adsorption−desorption isotherms of liquid nitrogen for two representative samples are reported. Similar to those in Figure 4b, they belong to type IV isotherms with a typical H4 hysteresis loop following IUPAC classification,[53] and the specific surface areas for the mesoporous SiO_2 sphere samples are 760.0 and 468.5 m^2/g (Table 1), respectively. Using the DDT and CTAB in our present soft-templating approach, once again, we have successfully maintained the porosity of SiO_2 hollow spheres in the same pore regime of 3.6 nm (i.e., diameter), as reported in Figure 7c (pore radius = 1.8 nm).

Our XPS analysis reveals that there is no inclusion of DDT in the as-prepared SiO_2−CTAB hybrid spheres (SI-3) because of absence of S 2p photoelectrons in the samples prepared with this route. A comparative thermogravimetric analysis (TGA) was further carried out for two types of mesoporous SiO_2 spheres prepared according to route (i) and route (iii) of Figure 1. In Figure 8a, small DrTGA peaks at 58.5 and 107 °C can be assigned to the evaporation of ethanol and moisture adsorbed on the large surfaces of SiO_2 spheres. The major weight loss at 245.0 °C is attributed to the decomposition of CTAB molecules, and another sharp weight decrease at the higher temperature of 308.8 °C is probably attributable to the decomposition of silanol or unhydrolyzed silane.[81] Similarly, in Figure 8b, the peak at

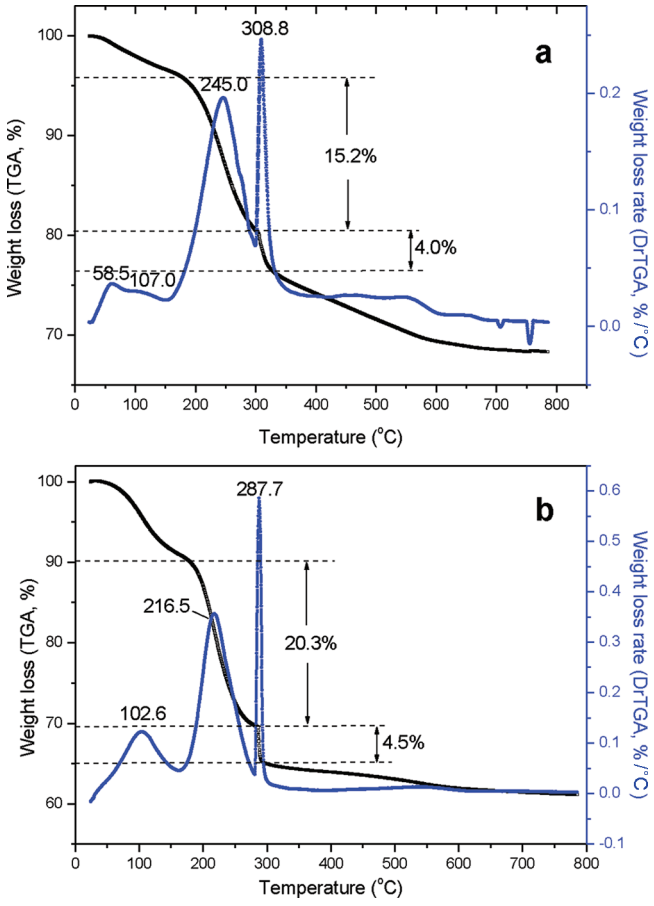

Figure 8. TGA and DrTGA curves of mesoporous SiO_2 spheres prepared according to (a) synthetic route (i) at 120 °C for 3 h and (b) synthetic route (iii) at 120 °C for 3 h (see Figure 1).

102.6 °C is ascribed to the evaporation of ethanol and moisture, and the peaks at 216.5 and 287.7 °C are due to the decomposition of organic surfactants and silanol/silane, respectively. It is interesting to note that all the major thermal events in the latter case have shifted to lower temperatures due to existence of shorter 1D-channels (Figure 6) when DDT is used in synthesis as a soft spherical template. Also quite interestingly, while the pore radii in these samples are essentially not changed (1.8 nm, Figure 7c, Table 1), their d_{10} spacing has a broader value at 4.5 nm (Figure 7b, Table 1), compared to those in Subsection 3.1 (3.5−3.6 nm, Table 1). Nevertheless, the value measured herein should not be overemphasized since the actual hexagonal structure of the 1D-assemblies of CTAB molecules is rather disordered (e.g., Figure 6i). Consistent with the TGA findings, the oxidative removal of CTAB assemblies from less ordered shell structures should also be easier. On the other hand, the nominal expansion in interplane distance could also be attributed to a weaker two-dimensional columnar interaction among the linear supramolecular assemblages of CTAB when they are in turn assembled perpendicularly on the existing spherical surface of the DDT templating droplets (i.e., micelles).

3.3. Architecture of Shell Structures. The above two types of mesoporous SiO_2 spheres are single-shelled. In order to illustrate synthetic flexibility of the present approaches, we have also investigated the effects of CTAB molecules on the architecture of shell structures in addition to their templating role for mesoporosity.

dx.doi.org/10.1021/cm201631m |*Chem. Mater.* 2011, 23, 4886–4899

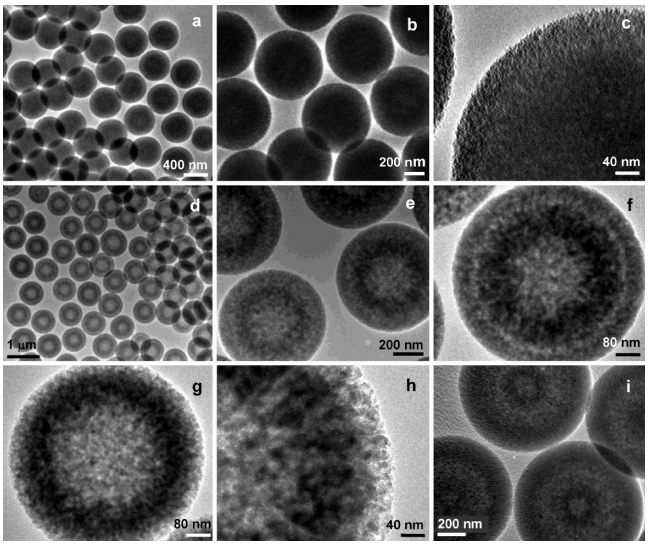

Figure 9. TEM images of mesoporous SiO_2 spheres prepared according to route (v) of Figure 1: (a-c) CTAB = 0.05 g and at 140 °C for 2 h, (d-f) CTAB = 0.05 g and at 180 °C for 4 h, (g-h) CTAB = 0.10 g and at 180 °C for 3 h, and (i) a modified route (v) (refer to SI-5).

More specifically, by adjusting the ratio of CTAB to TOES in synthesis, a third type of mesoporous SiO_2 products can be further obtained (route (v), Figure 1). In Figure 9, some of TEM images of this type of products are displayed. When the weight of CTAB in the starting precursor chemicals was reduced to 0.05 g, the spheres seem to divide into core (darker) and shell (lighter) regions as shown in the gray scales of the image contrasts (e.g., 140 °C, Figure 9a-c, where the average sphere size is 510 ± 12 nm). With longer reaction times or at higher temperatures (e.g., 180 °C, Figure 9d-f), hollowing the central core and generating the vacant space between the core and shell can be further attained, resulting in a double-shelled sphere morphology, where the mean diameter of the spheres is 657 ± 18 nm and their outer shell thickness is *ca.* 76 nm (Figure 9f). Keeping the reaction temperature constant while prolonging the reaction time, similar double-shelled SiO_2 spheres can also be obtained. To understand their formation mechanism, we had carried out a series of time-dependent experiments at 140 °C for 1, 2, and 6 h (TEM images of these samples are detailed in SI-4). After 1 h of reaction, no clear core−shell structure was obtained; instead, only solid spheres (i.e., the SiO_2−CTAB cores of Figure 5c(1)) were produced. At the time of 2 h, the shell phase was deposited on the core, and the image contrast of shell became much lighter and the center core was darker (Figure 5c(2)). This is a strong indication that the SiO_2 core and shell have different textures. It became more obvious at the time of 6 h that the shell was more separated and central hollow space further developed (Figure 5c(3)). The progressive generation of spaces in these double-shelled SiO_2 spheres can also be ascribed to the Ostwald ripening process, similar to those reported in Figures 2−4. When the weight of CTAB was gradually increased (e.g., 0.07 or 0.10 g), the boundary between the core and shell is less abrupt, and the final SiO_2 products should then be viewed as single-shelled spheres (Figure 9g-h). Nonetheless, the resultant shells in these spheres can still be divided into two different regions: the inner region is more compact, while the outer one is a bit loose, as can be seen from the image contrasts. When the CTAB finally

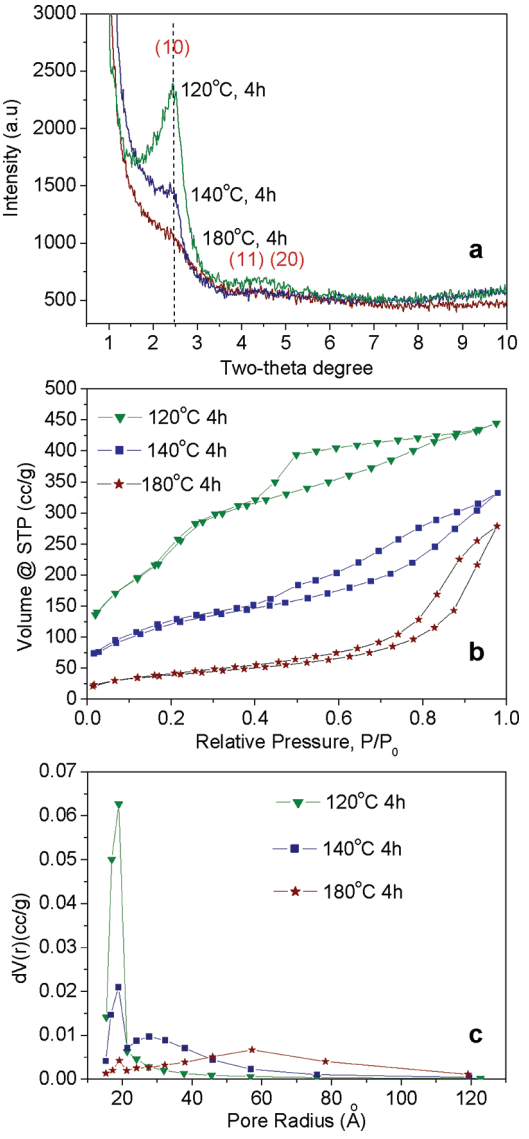

Figure 10. Characterization of mesoporous SiO_2 spheres synthesized at 120, 140, and 180 °C for 4 h according to route (v) of Figure 1: (a) XRD patterns (uncalcined samples), (b) nitrogen adsorption−desorption isotherms (calcined samples), and (c) pore radial distribution curves (BJH method).

reached 0.20 g, the hierarchical shell structure observed in Figure 9g-h returned back to the vertical cylindrical pore structure, as reported in Figures 2 to 4. Further modifications of shell architecture are still possible. For example, the intershell distance can be significantly enlarged by adding a small amount of sodium citrate in synthesis, as demonstrated in Figure 9i and detailed in SI-5. It should be pointed out that because of much smaller amounts of CTAB added in the syntheses of Figure 9, the flattening of spheres observed in SI-2 (Figure 5a) was not observed in this series of experiments. In fact, all the products are perfectly spherical.

Figure 10a reports the results of our XRD investigation for this type of mesoporous SiO_2 spheres. Despite the $d_{10} \approx 3.6$ nm for all the samples (Table 1), the spheres synthesized at 120 °C possess a higher degree of ordering of the hexagonal pore arrays, and this ordering gradually disappears as process temperature

dx.doi.org/10.1021/cm201631m |*Chem. Mater.* 2011, 23, 4886–4899

increases, judged by the relative intensities of (10) and (20) peaks.[82] At 140 °C, the (10) peak becomes weaker and the (20) disappears, indicating the presence of worm-hole-like pore structure instead of the long-range ordered array.[83,84] The regularity of hexagonal pore alignment is further deteriorated at 180 °C as the diffraction peak of (10) becomes virtually negligible. Under higher magnifications (SI-6), it is found the channel-like pores in the inner shells (i.e., located in the central core part) are straighter and more parallel to the radius of a sphere, compared to less aligned pores in the outer shells (Figure 9c and SI-6). Therefore, the intensities of diffraction peaks of Figure 10a are largely contributed by the better aligned mesopores in the inner shells. In this agreement, the adsorption−desorption isotherms of liquid nitrogen displayed in Figure 10b can also be classified to type IV isotherms with a typical H4 hysteresis loop (IUPAC classification).[53] Specific surface areas determined from BET analysis shown in Figure 10b are 924.9, 421.1, and 137.5 m^2/g for the samples prepared at 120, 140, and 180 °C respectively. The reduction in surface area upon the reaction temperature can be attributed to remarkable coarsening of the outer shell and hollowing of central core at a higher process temperature (e.g., 180 °C). In addition, Figure 10c shows that although all the samples have template pore radius located at *ca.* 1.9 nm, broader peaks appear at the pore radius of 2.8 or 5.8 nm in the samples made at 140 and 180 °C, respectively. Similar to those observed in Figure 4c, the population of pore radius at *ca.* 1.9 nm decreases, while those at 2.8 or 5.8 nm increase in these bimodal profiles, indicating that some of the pristine mesopores have merged or corrupted into bigger mesopores at higher process temperatures. Combining the TEM, BET/BJH, and XRD results together, it is known that reactions at higher temperatures are detrimental for the formation of CTAB-templated pores (radius = 1.9 nm). Because of insufficient templating support from the CTAB molecules, Ostwald ripening and SiO_2 condensation could take place more easily at higher temperatures, leading to less ordered pore structure and pore enlargement in the final products.

With the above temperature and time controlled experiments, we are now able to further address the growth mechanism of double-shelled mesoporous SiO_2 spheres. When a smaller amount of CTAB is used (i.e., under a larger TEOS/CTAB ratio than that used in route (i), Figure 1) in synthesis, normal SiO_2−CTAB hybrid spheres are still first formed, that is, TEOS molecules still hydrolyze among the CTAB rod-like templates according to route (i) of Figure 1. However, the remaining TEOS precursor would continue to hydrolyze and agglomerate/deposit onto the surface of the preformed SiO_2−CTAB cores, resulting in a CTAB-deficit SiO_2 shell. With an increase in temperature or reaction time, Ostwald ripening and coarsening processes greatly influence the final shell density and a clear interfacial void results. Similarly, an interior space is also generated in the central core, giving rise to the observed double-shelled structure. The above discussion can be better visualized with the schematic illustration in Figure 5c.

3.4. Encapsulation of Nanoparticles and Applications. With the inspiration of the concept of nanoreactors, we have encapsulated different functional materials (Au, Ag/Au, Ag, ZnS, TiO_2, Co_3O_4, and PAN) into the central spaces of the porous SiO_2 spheres (Figure 11a-f). There are two basic methods developed in this work which allow one to enwrap these functional materials. In the first one (*preinstalled method*), desired nanoparticles are mixed with starting synthetic precursor solutions, as

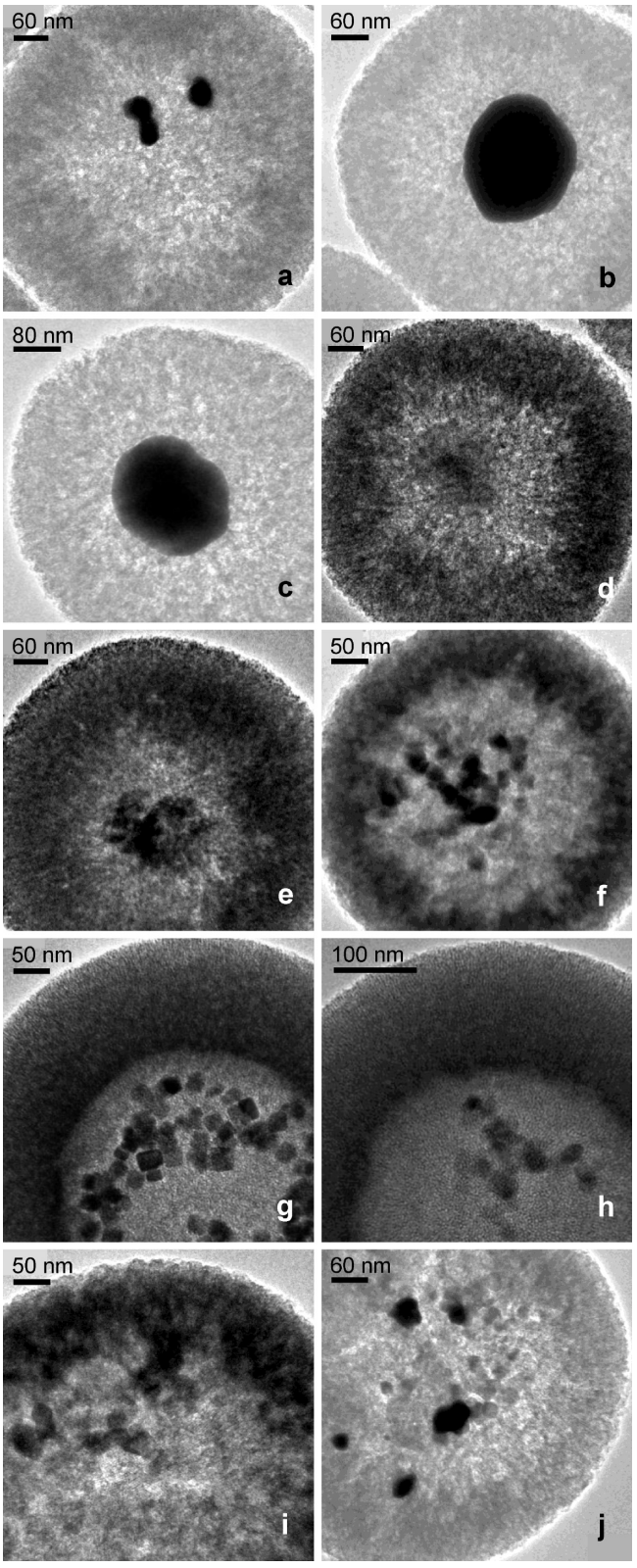

Figure 11. TEM images of ten encapsulated nanomaterials at SiO_2 (refer to Figure 1): (a) Au@SiO_2 (route (ii)), (b) Au@SiO_2 (route (i)), (c) Ag/Au@SiO_2 (route (i)), (d) PAN@SiO_2 (route (i)), (e) ZnS@SiO_2 (route (ii)), (f) Co_3O_4@SiO_2 (route (ii)), (g) Co_3O_4@SiO_2 (route (iv)), (h) TiO_2@SiO_2 (route (iv)), (i) TiO_2@SiO_2 (route (ii)), and (j) Au/TiO_2@SiO_2 (route (ii)).

dx.doi.org/10.1021/cm201631m |*Chem. Mater.* 2011, 23, 4886–4899

illustrated in routes (ii) and (iv) of Figure 1. In the second one (*on-site synthetic method*), the as-prepared hollow spheres of SiO_2 are used as empty "containers" (i.e., the SiO_2 hollow spheres prepared from the routes (i), (iii), and (v) of Figure 1) and the nanomaterials are then *on-site* synthesized in the central spaces. As shown in Figure 11a, multiple gold nanoparticles have been introduced successfully into the central part of the SiO_2 sphere. On the other hand, in Figure 11b, a single gold nanoparticle can be grown directly just inside a SiO_2 sphere according to route (i) of Figure 1. Compared with the external surface, as discussed earlier, the interior wall of the SiO_2 spheres is more reactive due to its surface roughness, which explains why the nucleation of gold clusters can be selectively taken place inside the containers. Since the subsequent growth is a diffusion controlled process through the shell channels, a singular particle is usually produced through this synthetic insertion. Moreover, the metal particles can occupy an entire space of the central void if desired, and in principle more complex nanoparticles can also be brought into the central space of SiO_2 spheres. In Figure 11c, for example, silver can also be coated onto a gold nanoparticle that has been pregrown (Figure 11b). These experiments collectively demonstrate that the interior and external spaces are interconnected well through the mesoporous channels of the SiO_2 shells.

In addition to the synthesis of inorganic materials, we further carried out organic synthesis inside these "nanoreactors". In particular, the polymerization of aniline was chosen to be a model reaction to elucidate the workability of the reactors. At first, monomer aniline dissolved in ethanol solvent was introduced to the porous SiO_2 spheres with assistance of ultrasonication. The chemical polymerization was then commenced with addition of initiators ammonium peroxydisulfate and hydrochloride acid. Figure 11d gives a PAN@SiO_2 sphere prepared according to this reaction approach (Figure 1(i) and SI-7). Similarly, the same polymerization can also be conducted inside the central spaces of the double-shelled SiO_2 spheres (Figure 1(v) and SI-7). However, due to the difficulty of the reactants in diffusing through the double shells, the polymerization could also take place outside the spheres. Besides the aniline polymerization in the liquid phase, the as-prepared PAN@SiO_2 organic−inorganic hybrid spheres were further tested for gas−solid reactions. Interestingly, the PAN solid can be completely removed through simple combustive oxidation in laboratory air at 500 °C, leaving the pure silica spheres intact (SI-7). Once again, the above liquid phase and gas phase reactions both confirm that the inner and outer spaces of the mesoporous SiO_2 spheres are indeed communicable.

Unlike the small noble metal nanoparticles, which are easy to fuse/agglomerate during the solvothermal treatments (e.g., Figure 11a), transition metal oxides and sulfides are relatively stable to sustain solid evacuation in the synthetic routes (ii) and (iv) depicted in Figure 1. In Figure 11f-g, two types of Co_3O_4@-SiO_2 nanocomposites synthesized according to the above two routes are displayed. As can be seen, the initial cubic shape of the Co_3O_4 powder remains unchanged after the solvothermal treatment. Similarly, two types of TiO_2@SiO_2 composite products are also reported in Figure 11h-i, respectively. The included TiO_2 powder with the size of around 30−40 nm can be observed in the central cavities, noting this size range is consistent with the average size of the as-received P25 powder. Finally, it should be mentioned that a second or even a third kind of nanoparticles can also be added into these SiO_2 spheres. In Figure 11j, we demonstrate that gold nanoparticles (AuNPs; with darker image contrasts) can be further introduced into the TiO_2@SiO_2 of Figure 11i, giving rise to a tertiary composite product of Au/TiO_2@SiO_2 (i.e., route (ii), Figure 1; see Subsection 2.6). This result elucidates that the TiO_2 nanoparticles inside the SiO_2 spheres were accessible to the $AuCl_4^-$ anions as well as other chemicals. With assistance of UV-light, the AuNPs could be grown directly on the surface of TiO_2 where opposite charge carriers (electrons and holes) were available upon the UV-photon irradiation.[85] Indirectly, it can also be deduced that the TiO_2 nanoparticles were not coated with a thin layer of silica, because they remained active after the preparation. In our experiments through route (ii), Figure 1, we found that the encapsulated nanoparticles are not imbedded in the shell structures (i.e., not stuck inside the 1D-channels). In this regard, the nanoparticles may largely agglomerate in the centers of the SiO_2−CTAB hybrid gel spheres prior to the Ostwald ripening process and therefore they may also serve as nuclei for condensation of the SiO_2−CTAB phase during the vertical channel growth (route (ii), Figure 1). On the other hand, the nanoparticles may be well dispersed within the micellar phase (i.e., "oil" phase of DDT), which would naturally lead to center-inclusive configurations as evidenced in Figure 11g-h (also refer to route (iv), Figure 1). Furthermore, we do not notice obvious growth of nanoparticles within the porous channels (Figure 11b,c,d,j) using the *on-site* synthetic methods (such as routes (i), (iii) and (v), Figure 1), which suggests that these channels solely serve as entrance or exit for the ionic and molecular species during the chemical reactions.

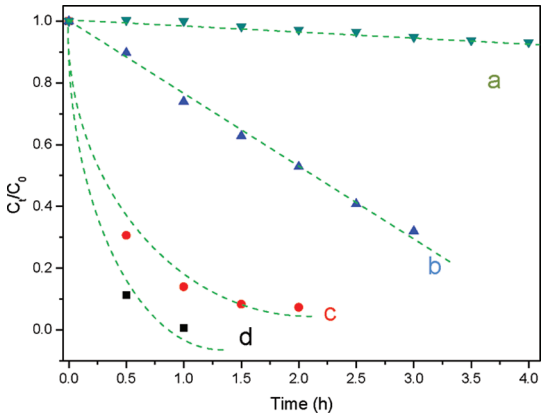

Figure 12. Photocatalysis data with normalized concentration (C_t/C_0; C_0 and C_t are initial concentration and concentration at time t of methyl orange) versus reaction time (t in hours) for the four catalysts used in the experiments: (a) mesoporous SiO_2 spheres (route (iii) of Figure 1; 10 mg) without TiO_2 (P25), (b) calcined TiO_2@SiO_2 spheres (route (iv) of Figure 1, also see Figure 11(h); 10 mg, TiO_2 = 1.3 mg and SiO_2 = 8.7 mg), (c) 1.3 mg of calcined P25 powder physically mixed with 8.7 mg mesoporous SiO_2 spheres (route (iii) of Figure 1), and (d) 1.3 mg of calcined P25 powder.

Apart from the photoinduced synthetic reactions inside the central cavity, we have also carried out photocatalytic reactions inside the as-prepared TiO_2@SiO_2 "nanoreactors" (Figure 11h; see route (iv) of Figure 1). In particular, photocatalytic degradation of methyl orange (MO) was chosen as another model reaction for demonstrative purposes.[86] Figure 12 reports some kinetic data from this investigation (see Subsection 2.6). In order to minimize the effect of adsorption of MO molecules onto the large surface of SiO_2 shells, the starting concentration of C_0 is the

value after adsorption equilibrium has reached (24 h); in general, the adsorption of MO on the SiO_2 spheres is quite minor (see SI-8). From these graphs, we can see that mesoporous SiO_2 spheres have negligible catalytic activity toward MO (curve a), while the TiO_2 (P25) nanoparticles have the highest activity. On the other hand, P25 can degrade all MO molecules just within 1 h (curve d), and, similarly, a physically mixed sample of P25 and mesoporous SiO_2 spheres also shows high photocatalytic activity (curve c), but because blockage of UV light by the larger SiO_2 spheres, the activity of P25 nanoparticles in this case has been reduced to some extent. In comparison, our mesoporous TiO_2@SiO_2 spheres also give reasonable photocatalytic activity. As shown in curve b, their activity is not as high as unconfined TiO_2 nanoparticles (see curves c and d), because the MO molecules must diffuse through the mesoporous channels in order to access TiO_2 nanoparticles. Furthermore, the intensity of UV light in the interior space is not as strong, due to the light scattering and blockage by the SiO_2 channel walls and shells. Importantly, nevertheless, this investigation elucidates that the UV light can penetrate or scatter through the porous SiO_2 shells and provide the needed photon energy to the TiO_2 catalyst loaded in the interior spaces. At the same time, it also indicates that the organic dye molecules can diffuse through the vertical channels and reach the photon-excited TiO_2 nanoparticles. Due to the presence of active free radical species and charged carriers on the TiO_2 surfaces, one can observe a significant difference in degradation performance when the experiments were carried out with or without the presence of TiO_2 catalysts. Because the uniform pore size for the silica shells is around 3.6 nm, this type of TiO_2@SiO_2 nanoreactors will only allow the molecules smaller than this size limit to enter the central interior. For example, in the present case, the long axis of MO molecules is estimated to be 1.3 nm,[87] which is around 1/3 of the pore size and the molecules can indeed reach the TiO_2 catalyst in the center. In this sense, our TiO_2@SiO_2 spheres can also work as inorganic membrane reactors with additional functions of size selectivity. Similar investigations should also be extended in the future to other mesoporous SiO_2-based nanocomposite systems, in addition to those reported in Figure 11.

4. CONCLUSIONS

In summary, we have developed three simple one-pot solvothermal methods for preparation of mesoporous SiO_2 hollow spheres with hexagonally aligned 1D-channels toward the center of sphere. Using the EG−CTAB−water as a reaction medium, hollow interiors can be gradually evolved inside the SiO_2 spheres through the Ostwald ripening mechanism, through which both reaction time and temperature can be utilized as controlling process parameters. Using the EG− CTAB−DDT−water as a reaction system, on the other hand, smoother interior walls for the central cavities of SiO_2 spheres can be attained, where the DDT phase serves as a soft-template (i.e., micelles) for deposition of the SiO_2−CTAB hybrid. With a smaller amount of CTAB molecules used in synthesis, double-shelled SiO_2 spheres can be further engineered. Because their vertical 1D-channels offer the shortest pathway for ionic and/or molecular chemical species and their hollow interiors provide an essential space for chemical reactions, the above prepared SiO_2 spheres could further function as ideal nanoreactors. Furthermore, size-selective reactions can also be realized by controlling diameters of the 1D-channels. In addition to the synthesis of the phase-pure SiO_2 spheres, we have also devised two solution-based methods, *pre-installation* and *on-site synthesis*, to introduced functional materials into the central cavities of SiO_2 spheres. In particular, nanoparticles such as TiO_2, Co_3O_4, ZnS, Au, Ag/Au, and polyaniline etc. have been introduced into the interior spaces of the mesoporous SiO_2 spheres, and a total of 10 such SiO_2-based nanocomposites have been exemplified in this work. The above synthetic methods indeed demonstrate their methodological merits and generality for design and architecture of this class of porous SiO_2-enwrapped functional materials. Moreover, communicable 1D-channels of the SiO_2 shells and workability of the enclosed nanomaterials have also been verified with the photocatalytic degradation of organic dyes (e.g., methyl orange) and oxidative combustions of polyaniline. On the basis of the above chemical reactions, it has been unambiguously proven that both inorganic ions and organic molecular species can penetrate through the 1D-channels and react within the interior spaces of SiO_2 spheres, including deposition on preexisting solid phases. Importantly, our spherical SiO_2 products can be broadly classified into five major structural forms, and the mean diameters of the 1D-channels in the shells are all constantly in the range of 3.6−3.8 nm for the SiO_2 spheres as well as SiO_2-enwrapped functional materials. In view of their working flexibility, we believe that the synthetic approaches and general concepts developed should also be applicable to the preparation of other advanced composite materials, in addition to those reported in the current work.

■ ASSOCIATED CONTENT

Supporting Information. TEM, SAED, and XPS results (PDF). This material is available free of charge via the Internet at http://pubs.acs.org.

■ AUTHOR INFORMATION

Corresponding Author

*Phone: (65) 6516-2896. Fax: (65) 6779-1936. E-mail: chezhc@nus.edu.sg.

■ ACKNOWLEDGMENT

The authors gratefully acknowledge the Economic Development Board, Singapore and King Abdullah University of Science and Technology, Saudi Arabia for support of this research. D.P. W. would also like to thank the National University of Singapore for providing her postgraduate scholarship.

■ REFERENCES

(1) Kresge, C. T.; Leonowicz, M. E.; Roth, W. J.; Vartuli, J. C.; Beck, J. S. *Nature* **1992**, *359*, 710–712.
(2) Lin, H.-P.; Cheng, S.; Mou, C.-Y. *Chem. Mater.* **1998**, *10*, 581–589.
(3) Lin, H.-P.; Cheng, Y.-R.; Mou, C.-Y. *Chem. Mater.* **1998**, *10*, 3772–3776.
(4) Yang, P. D.; Zhao, D. Y.; Margolese, D. I.; Chmelka, B. F.; Stucky, G. D. *Nature* **1998**, *396*, 152–155.
(5) Zhao, D.; Huo, Q.; Feng, J.; Chmelka, B. F.; Stucky, G. D. *J. Am. Chem. Soc.* **1998**, *120*, 6024–6036.
(6) Zhao, D. Y.; Feng, J. L.; Huo, Q. S.; Melosh, N.; Fredrickson, G. H.; Chmelka, B. F.; Stucky, G. D. *Science* **1998**, *279*, 548–552.
(7) Jun, S.; Joo, S. H.; Ryoo, R.; Kruk, M.; Jaroniec, M.; Liu, Z.; Ohsuna, T.; Terasaki, O. *J. Am. Chem. Soc.* **2000**, *122*, 10712–10713.

(8) (a) Caruso, F.; Shi, X. Y.; Caruso, R. A.; Susha, A. *Adv. Mater.* **2001**, *13*, 740–744. (b) Bagshaw, S. A.; Hayman, A. R. *Adv. Mater.* **2001**, *13*, 1011–1013.
(9) (a) Ryoo, R.; Park, I.-S.; Jun, S.; Lee, C. W.; Kruk, M.; Jaroniec, M. *J. Am. Chem. Soc.* **2001**, *123*, 1650–1657. (b) Lee, J.-S.; Joo, S. H.; Ryoo, R. *J. Am. Chem. Soc.* **2002**, *124*, 1156–1157.
(10) Lin, H.-P.; Mou, C.-Y. *Acc. Chem. Res.* **2002**, *35*, 927–935.
(11) Yu, C.; Tian, B.; Fan, J.; Stucky, G. D.; Zhao, D. *J. Am. Chem. Soc.* **2002**, *124*, 4556–4557.
(12) (a) Wang, J.; Zhang, J.; Asoo, B. Y.; Stucky, G. D. *J. Am. Chem. Soc.* **2003**, *125*, 13966–13967. (b) Meng, X.; Di, Y.; Zhao, L.; Jiang, D.; Li, S.; Xiao, F.-S. *Chem. Mater.* **2004**, *16*, 5518–5526.
(13) (a) Lin, Y.-S.; Tsai, C.-P.; Huang, H.-Y.; Kuo, C.-T.; Hung, Y.; Huang, D.-M.; Chen, Y.-C.; Mou, C.-Y. *Chem. Mater.* **2005**, *17*, 4570–4573. (b) Lin, Y. S.; Wu, S. H.; Tseng, C. T.; Hung, Y.; Chang, C.; Mou, C. Y. *Chem. Commun.* **2009**, 3542–3544.
(14) Wan, Y.; Zhao, D. *Chem. Rev.* **2007**, *107*, 2821–2860.
(15) Chen, H. M.; He, J. H.; Tang, H. M.; Yan, C. X. *Chem. Mater.* **2008**, *20*, 5894–5900.
(16) Gaslain, F. O. M.; Delacote, C.; Walcarius, A.; Lebeau, B. *J. Sol-Gel Sci. Technol.* **2009**, *49*, 112–124.
(17) Lee, H. I.; Kim, J. M.; Stucky, G. D. *J. Am. Chem. Soc.* **2009**, *131*, 14249–14251.
(18) Lin, H. M.; Zhu, G. S.; Xing, J. J.; Gao, B.; Qiu, S. L. *Langmuir* **2009**, *25*, 10159–10164.
(19) Kobler, J.; Bein, T. *ACS Nano* **2008**, *2*, 2324–2330.
(20) Han, Y.-J.; Stucky, G. D.; Butler, A. *J. Am. Chem. Soc.* **1999**, *121*, 9897–9898.
(21) Bibby, A.; Mercier, L. *Chem. Mater.* **2002**, *14*, 1591–1597.
(22) Darga, A.; Kecht, J.; Bein, T. *Langmuir* **2007**, *23*, 12915–12922.
(23) Zhang, W.-H.; Zhang, X.; Hua, Z.; Harish, P.; Schroeder, F.; Hermes, S.; Cadenbach, T.; Shi, J.; Fischer, R. A. *Chem. Mater.* **2007**, *19*, 2663–2670.
(24) Zhu, Y.; Kaskel, S.; Shi, J.; Wage, T.; van Pée, K.-H. *Chem. Mater.* **2007**, *19*, 6408–6413.
(25) Kecht, J.; Bein, T. *Langmuir* **2008**, *24*, 14209–14214.
(26) Barczak, M.; Pikus, S.; Skrzydlo-Radomanska, B.; Dabrowski, A. *Adsorpt.-J. Int. Adsorpt. Soc.* **2009**, *15*, 278–286.
(27) Wan, Y.; Wang, H.; Zhao, Q.; Klingstedt, M.; Terasaki, O.; Zhao, D. *J. Am. Chem. Soc.* **2009**, *131*, 4541–4550.
(28) Hentze, H.-P.; Raghavan, S. R.; McKelvey, C. A.; Kaler, E. W. *Langmuir* **2003**, *19*, 1069–1074.
(29) Yano, K.; Fukushima, Y. *J. Mater. Chem.* **2004**, *14*, 1579–1584.
(30) Xu, D.; Liu, Z. P.; Liang, J. B.; Qian, Y. T. *J. Phys. Chem. B* **2005**, *109*, 14344–14349.
(31) Yeh, Y.-Q.; Chen, B.-C.; Lin, H.-P.; Tang, C.-Y. *Langmuir* **2005**, *22*, 6–9.
(32) Zhao, W.; Gu, J.; Zhang, L.; Chen, H.; Shi, J. *J. Am. Chem. Soc.* **2005**, *127*, 8916–8917.
(33) Zhu, Y. F.; Shi, J. L.; Shen, W. H.; Chen, H. R.; Dong, X. P.; Ruan, M. L. *Nanotechnology* **2005**, *16*, 2633–2638.
(34) Wang, J. G.; Xiao, Q.; Zhou, H. J.; Sun, P. C.; Yuan, Z. Y.; Li, B. H.; Ding, D. T.; Shi, A. C.; Chen, T. H. *Adv. Mater.* **2006**, *18*, 3284–3288.
(35) Blas, H.; Save, M.; Pasetto, P.; Boissiere, C.; Sanchez, C.; Charleux, B. *Langmuir* **2008**, *24*, 13132–13137.
(36) Feng, Z. G.; Li, Y. S.; Niu, D. C.; Li, L.; Zhao, W. R.; Chen, H. R.; Gao, J. H.; Ruan, M. L.; Shi, J. L. *Chem. Commun.* **2008**, 2629–2631.
(37) Joo, S. H.; Park, J. Y.; Tsung, C. K.; Yamada, Y.; Yang, P. D.; Somorjai, G. A. *Nat. Mater.* **2009**, *8*, 126–131.
(38) Pan, D. H.; Yuan, P.; Zhao, L. Z.; Liu, N. A.; Zhou, L.; Wei, G. F.; Zhang, J.; Ling, Y. C.; Fan, Y.; Wei, B. Y.; Liu, H. Y.; Yu, C. Z.; Bao, X. J. *Chem. Mater.* **2009**, *21*, 5413–5425.
(39) Zhang, A. F.; Zhang, Y. C.; Xing, N.; Hou, K. K.; Guo, X. W. *Chem. Mater.* **2009**, *21*, 4122–4126.
(40) Caruso, F.; Caruso, R. A.; Mohwald, H. *Chem. Mater.* **1999**, *11*, 3309–3314.
(41) Caruso, F. *Adv. Mater.* **2001**, *13*, 11–22.
(42) Liang, Z. J.; Susha, A.; Caruso, F. *Chem. Mater.* **2003**, *15*, 3176–3183.
(43) Wang, Y. J.; Caruso, F. *Chem. Commun.* **2004**, 1528–1529.
(44) Liu, S. H.; Han, M. Y. *Adv. Funct. Mater.* **2005**, *15*, 961–967.
(45) Liu, S. H.; Zhang, Z. H.; Han, M. Y. *Adv. Mater.* **2005**, *17*, 1862–1866.
(46) Arnal, P. M.; Comotti, M.; Schuth, F. *Angew. Chem., Int. Ed.* **2006**, *45*, 8224–8227.
(47) Dong, X.; Chen, H.; Zhao, W.; Li, X.; Shi, J. *Chem. Mater.* **2007**, *19*, 3484–3490.
(48) Liu, S. H.; Wong, Y.; Wang, Y. B.; Wang, D. S.; Han, M. Y. *Adv. Funct. Mater.* **2007**, *17*, 3147–3152.
(49) Yang, J.; Lee, J.; Kang, J.; Lee, K.; Suh, J.-S.; Yoon, H.-G.; Huh, Y.-M.; Haam, S. *Langmuir* **2008**, *24*, 3417–3421.
(50) Deng, Y.; Qi, D.; Deng, C.; Zhang, X.; Zhao, D. *J. Am. Chem. Soc.* **2008**, *130*, 28–29.
(51) (a) Fuertes, M. C.; Marchena, M.; Marchi, M. C.; Wolosiuk, A.; Soler-Illia, G. *Small* **2009**, *5*, 272–280. (b) Wu, X.-J.; Xu, D. *J. Am. Chem. Soc.* **2009**, *131*, 2774–2775.
(52) (a) Liu, J. A.; Qiao, S. Z.; Hartono, S. B.; Lu, G. Q. *Angew. Chem., Int. Ed.* **2010**, *49*, 4981–4985. (b) Liu, J.; Hartono, S. B.; Jin, Y. G.; Li, Z.; Lu, G. Q.; Qiao, S. Z. *J. Mater. Chem.* **2010**, *20*, 4595–4601. (c) Qiao, S. Z.; Lin, C. X.; Jin, Y. G.; Li, Z.; Yan, Z. M.; Hao, Z. P.; Huang, Y. N.; Lu, G. Q. *J. Phys. Chem. C* **2009**, *113*, 8673–8682. (d) Liu, J.; Fan, F.; Feng, Z.; Zhang, L.; Bai, S.; Yang, Q.; Li, C. *J. Phys. Chem. C* **2008**, *112*, 16445–16451. (e) Liu, J.; Yang, Q. H.; Zhang, L.; Yang, H. Q.; Gao, J. S.; Li, C. *Chem. Mater.* **2008**, *20*, 4268–4275. (f) Liu, J.; Bai, S. Y.; Zhong, H.; Li, C.; Yang, Q. H. *J. Phys. Chem. C* **2010**, *114*, 953–961. (g) Zhao, W. R.; Gu, J. L.; Zhang, L. X.; Chen, H. R.; Shi, J. L. *J. Am. Chem. Soc.* **2005**, *127*, 8916–8917. (h) Chen, Y.; Chen, H. R.; Guo, L. M.; He, Q. J.; Chen, F.; Zhou, J.; Feng, J. W.; Shi, J. L. *ACS Nano* **2010**, *4*, 529–539.
(53) Sing, K. S. W.; Everett, D. H.; Haul, R. A. W.; Moscou, L.; Pierotti, R. A.; Rouquerol, J.; Siemieniewska, T. *Pure Appl. Chem.* **1985**, *57*, 603–619.
(54) Feng, J.; Zeng, H. C. *Chem. Mater.* **2003**, *15*, 2829–2835.
(55) Yu, X. X.; Yu, J. G.; Cheng, B.; Huang, B. B. *Chem.—Eur. J.* **2009**, *15*, 6731–6739.
(56) Enüstün, B. V.; Turkevich, J. *J. Am. Chem. Soc.* **1963**, *85*, 3317–3328.
(57) Ostwald, W. *Z. Phys. Chem.* **1900**, *34*, 495–503.
(58) Yang, H. G.; Zeng, H. C. *J. Phys. Chem. B* **2004**, *108*, 3492–3495.
(59) Zeng, H. C. *J. Mater. Chem.* **2006**, *16*, 649–662.
(60) Chang, Y.; Teo, J. J.; Zeng, H. C. *Langmuir* **2005**, *21*, 1074–1079.
(61) Zhang, Y.; Li, G.; Wu, Y.; Luo, Y.; Zhang, L. *J. Phys. Chem. B* **2005**, *109*, 5478–5481.
(62) Liu, B.; Zeng, H. C. *Small* **2005**, *1*, 566–571.
(63) (a) Li, J.; Zeng, H. C. *Angew. Chem., Int. Ed.* **2005**, *44*, 4342–4345. (b) Li, J.; Zeng, H. C. *J. Am. Chem. Soc.* **2007**, *129*, 15839–15847.
(64) Teo, J. J.; Chang, Y.; Zeng, H. C. *Langmuir* **2006**, *22*, 7369–7377.
(65) Wang, Y.; Zhu, Q.; Zhang, H. *Chem. Commun.* **2005**, *41*, 5231–5233.
(66) Zheng, Y.; Cheng, Y.; Wang, Y.; Zhou, L.; Bao, F.; Jia, C. *J. Phys. Chem. B* **2006**, *110*, 8284–8288.
(67) Cao, X.; Gu, L.; Zhuge, L.; Gao, W.; Wang, W.; Wu, S. *Adv. Funct. Mater.* **2006**, *16*, 896–902.
(68) Li, B.; Rong, G.; Xie, Y.; Huang, L.; Feng, C. *Inorg. Chem.* **2006**, *45*, 6404–6410.
(69) Zhang, H.; Qi, L. *Nanotechnology* **2006**, *17*, 3984–3988.
(70) Xu, H.; Wang, W.; Zhu, W.; Zhou, L. *Nanotechnology* **2006**, *17*, 3649–3654.
(71) Lou, X. W.; Wang, Y.; Lee, J. Y.; Archer, L. A. *Adv. Mater.* **2006**, *18*, 2325–2329.

(72) Yu, J.; Guo, H.; Davis, S. A.; Mann, S. *Adv. Funct. Mater.* **2006**, *16*, 2035–2041.
(73) Wang, W.-S.; Zhen, L.; Xu, C.-Y.; Zhang, B.-Y.; Shao, W.-Z. *J. Phys. Chem. B* **2006**, *110*, 23154–23158.
(74) Huang, J.; Gao, L. *J. Am. Ceram. Soc.* **2006**, *89*, 3887–3880.
(75) Cheng, Y.; Wang, Y.; Jia, C.; Bao, F. *J. Phys. Chem. B* **2006**, *110*, 24399–24402.
(76) Zeng, H. C. *J. Mater. Chem.* **2011**, *21*, 7511–7526.
(77) Cheng, H. Q.; Tamaki, R.; Laine, R. M.; Babonneau, F.; Chujo, Y.; Treadwell, D. R. *J. Am. Chem. Soc.* **2000**, *122*, 10063–10072.
(78) (a) Zhang, Y. X.; Zeng, H. C. *Adv. Mater.* **2009**, *21* (48), 4962–4965. (b) Cha, S.-H.; Kim, K.-H.; Kim, J.-U.; Lee, W.-K.; Lee, J.-C. *J. Phys. Chem. C* **2008**, *112*, 13862–13868.
(79) Wan, Y.; Yu, S. H. *J. Phys. Chem. C* **2008**, *112*, 3641–3647.
(80) Wang, H.; Yu, M.; Lin, C.; Liu, X. M.; Lin, J. *J. Phys. Chem. C* **2007**, *111*, 11223–11230.
(81) Chen, M.; Wu, L. M.; Zhou, S. X.; You, B. *Adv. Mater.* **2006**, *18*, 801–806.
(82) Fan, J.; Boettcher, S. W.; Stucky, G. D. *Chem. Mater.* **2006**, *18*, 6391–6396.
(83) Ismail, A. A.; Bahnemann, D. W.; Robben, L.; Yarovyi, V.; Wark, M. *Chem. Mater.* **2009**, *21*, 2601–2603.
(84) El-Safty, S. A.; Prabhakaran, D.; Ismail, A. A.; Matsunaga, H.; Mizukami, F. *Chem. Mater.* **2008**, *20*, 2644–2654.
(85) Li, J.; Tang, S. B.; Lu, L.; Zeng, H. C. *J. Am. Chem. Soc.* **2007**, *129*, 9401–9409.
(86) Liu, B.; Zeng, H. C. *Chem. Mater.* **2008**, *20*, 2711–2718.
(87) Takahashi, M.; Kobayashi, K.; Takaoka, K.; Tajima, K. *Thin Solid Films* **1997**, *307*, 274–279.